

1 **Impacts of aerosol-photolysis interaction and aerosol-radiation**
2 **feedback on surface-layer ozone in North China during multi-**
3 **pollutant air pollution episodes**

4

5 Hao Yang¹, Lei Chen¹, Hong Liao¹, Jia Zhu¹, Wenjie Wang², Xin Li²

6

7 ¹Jiangsu Key Laboratory of Atmospheric Environment Monitoring and Pollution
8 Control, Jiangsu Collaborative Innovation Center of Atmospheric Environment and
9 Equipment Technology, School of Environmental Science and Engineering,
10 Nanjing University of Information Science & Technology, Nanjing 210044, China

11 ²State Joint Key Laboratory of Environmental Simulation and Pollution Control,
12 College of Environmental Sciences and Engineering, Peking University, Beijing
13 100871, China

14

15 **Correspondence:** Lei Chen (chenlei@nuist.edu.cn) and Hong Liao
16 (hongliao@nuist.edu.cn)

17

Abstract

We examined the impacts of aerosol-radiation interactions, including the effects of aerosol-photolysis interaction (API) and aerosol-radiation feedback (ARF), on surface-layer ozone (O_3) concentrations during three multi-pollutant air pollution episodes characterized by high O_3 and $PM_{2.5}$ levels during 28 July to 3 August 2014 (Episode1), 8-13 July 2015 (Episode2) and 5-11 June 2016 (Episode3) in North China, by using the Weather Research and Forecasting with Chemistry (WRF-Chem) model embedded with an integrated process analysis scheme. Our results show that aerosol-radiation interactions decreased the daytime shortwave radiation at surface by $92.4\sim 100.3\text{ W m}^{-2}$ averaged over the complex air pollution areas in these three episodes. The dimming effect reduced the near-surface photolysis rates of $J[NO_2]$ and $J[O^1D]$ by $1.8 \times 10^{-3}\sim 2.0 \times 10^{-3}\text{ s}^{-1}$ and $5.7 \times 10^{-6}\sim 6.3 \times 10^{-6}\text{ s}^{-1}$, respectively. However, the daytime shortwave radiation in the atmosphere was increased by $72.8\sim 85.2\text{ W m}^{-2}$, which made the atmosphere more stable. The stabilized atmosphere decreased the planetary boundary layer height and 10 m wind speed by $129.0\sim 249.0\text{ m}$ and $0.05\sim 0.12\text{ m s}^{-1}$, respectively. The weakened photolysis rates and changed meteorological conditions reduced daytime surface-layer O_3 concentrations by up to $9.3\sim 11.4\text{ ppb}$, with API and ARF contributing $74.6\%\sim 90.0\%$ and $10.0\%\sim 25.4\%$ of the O_3 decrease in these three episodes, respectively. Process analysis indicated that the weakened O_3 chemical production made the greatest contribution to API effect while the reduced vertical mixing was the key process for ARF effect. This study implies that future $PM_{2.5}$ reductions will lead to O_3 increases due to weakened aerosol-radiation interactions. Therefore, tighter controls of O_3 precursors are needed to offset O_3 increases caused by weakened aerosol-radiation interactions in the future.

1 Introduction

China has been experiencing severe air pollution in recent years, characterized by high loads of PM_{2.5} (particulate matter with an aerodynamic equivalent diameter of 2.5 micrometers or less) and high levels of ozone (O₃). Observational studies exhibited positive correlations and synchronous occurrence of PM_{2.5} and O₃ pollution in North China during summer (Zhao et al., 2018; Zhu et al., 2019), indicating that complex air pollution is becoming a major challenge for North China.

Aerosols can absorb and scatter solar radiation to affect Earth's energy balance. They can also act as cloud condensation nuclei and ice nuclei, and further modify the microphysical characteristics of clouds (Albrecht et al., 1989; Haywood et al., 2000; Lohmann et al., 2005). Both ways perturb meteorological variables, e.g., temperature, planetary boundary layer height (PBLH), and precipitation, and eventually influence air pollutants (Petäjä et al., 2016; Miao et al., 2018; Zhang et al., 2018). Many studies are focused on the feedback between aerosol and meteorology (Gao et al., 2015; Gao et al., 2016a; Qiu et al., 2017; Chen et al., 2019; Zhu et al., 2021). Gao et al. (2015) used the WRF-Chem model to investigate the feedbacks between aerosols and meteorological variables over the North China Plain in January 2013, and pointed out that aerosols could cause a decrease in surface temperature by 0.8-2.8 °C but an increase of 0.1-0.5 °C around 925 hPa. The more stable atmosphere caused by surface cooling and higher layer heating led to the decreases of surface wind speed and PBLH by 0.3 m s⁻¹ and 40-200 m, respectively, which further resulted in overall PM_{2.5} increases by 10-50 µg m⁻³ (2-30%). By using the same WRF-Chem model, Qiu et al. (2017) reported that the surface downward shortwave radiation and PBLH were reduced by 54.6 W m⁻² and 111.4 m due to aerosol radiative forcing during 21 and 27 February 2014 in the North China Plain. As a result, the surface PM_{2.5} concentration averaged over the North China Plain was increased by 34.9 µg m⁻³ (20.4%).

Aerosols can also influence O₃ through aerosol-radiation interactions, including aerosol-photolysis interaction and aerosol-radiation feedback. Aerosols can scatter and absorb UV radiation, and therefore directly affect O₃ photochemistry reactions,

which is called aerosol-photolysis interaction (API) (Dickerson et al., 1997; Liao et al., 1999; Li et al., 2011; Lou et al., 2014). The changed meteorological variables due to aerosol radiative forcing can indirectly affect O₃ concentrations, which is called aerosol-radiation feedback (ARF) (Hansen et al., 1997; Gao et al., 2018; Liu et al., 2020). Although the effects of API or ARF on O₃ have been examined by previous studies (Xing et al., 2017; Gao et al., 2018; Gao et al., 2020), the combined effects of API and ARF on O₃, especially under the conditions of synchronous occurrence of high PM_{2.5} and O₃ concentrations, remain largely elusive.

The present study aims to (1) quantify the respective/combined contributions of API and ARF on surface O₃ concentrations by using the WRF-Chem model; (2) explore the prominent physical and/or chemical processes responsible for API and ARF effects by using an integrated process rate (IPR) analysis embedded in WRF-Chem model. In order to draw the general conclusions, three multi-pollutant air pollution episodes characterized by high O₃ and PM_{2.5} levels during 28 July to 3 August 2014 (Episode1), 8-13 July 2015 (Episode2) and 5-11 June 2016 (Episode3) in North China are analyzed in this study. The model configuration, numerical experiments, observational data, and the integrated process rate analysis are described in section 2. Section 3 shows the model evaluation. The presentation and discussion of the model results are exhibited in section 4, and the conclusions and discussions are provided in section 5.

2 Methods

2.1 Model configuration

The version 3.7.1 of the online-coupled Weather Research and Forecasting with Chemistry (WRF-Chem) model (Grell et al., 2005; Skamarock et al., 2008) is used in this study to explore the impacts of aerosol-radiation interactions on surface-layer O₃ in North China. WRF-Chem can simulate gas phase species and aerosols coupled with meteorological fields, and has been widely used to investigate air pollution over North China (Gao et al., 2016a; Gao et al., 2020; Wu et al., 2020). As shown in Fig. 1, we design two nested model domains with the number of grid points of 57 (west-east) ×

41 (south–north) and 37 (west–east) \times 43 (south–north) at 27 and 9 km horizontal resolutions, respectively. The parent domain centers at (39 °N, 117 °E). The model contains 29 vertical levels from the surface to 50 hPa, with 14 levels below 2 km for the fully description of the vertical structure of planetary boundary layer (PBL).

The Carbon Bond Mechanism Z (CBM-Z) is selected as the gas-phase chemical mechanism (Zaveri and Peters, 1999), and the full 8-bin MOSAIC (Model for Simulating Aerosol Interactions and Chemistry) aerosol module with aqueous chemistry is used to simulate aerosol evolution (Zaveri et al., 2008). The photolysis rates are calculated by the Fast-J scheme (Wild et al., 2000). Other major physical parameterizations used in this study are listed in Table 1.

The initial and boundary meteorological conditions are provided by the National Centers for Environmental Prediction (NCEP) Final Analysis data with a spatial resolution of $1^\circ \times 1^\circ$. In order to limit the model bias of simulated meteorological fields, the four-dimensional data assimilation (FDDA) is used with the nudging coefficient of 3.0×10^{-4} for wind, temperature and humidity (no analysis nudging is applied for the inner domain) (Lo et al., 2008; Otte, 2008). Chemical initial and boundary conditions are obtained from the Model for Ozone and Related chemical Tracers, version 4 (MOZART-4) forecasts (Emmons et al., 2010).

Anthropogenic emissions in Episode1 are taken from the 2010 MIX Asian emission inventory, and the Multi-resolution Emission Inventory for China (MEIC) is used in Episode2 and Episode3 (<http://www.meicmodel.org/>) (Li et al., 2017a). These emission inventories provide emissions of sulfur dioxide (SO₂), nitrogen oxides (NO_x), carbon monoxide (CO), non-methane volatile organic compounds (NMVOCs), carbon dioxide (CO₂), ammonia (NH₃), black carbon (BC), organic carbon (OC), PM₁₀ (particulate matter with aerodynamic diameter is 10 μ m and less) and PM_{2.5}. Emissions are aggregated from four sectors, including power generation, industry, residential, and transportation, with $0.25^\circ \times 0.25^\circ$ spatial resolution. Biogenic emissions are calculated online by the Model of Emissions of Gases and Aerosols from Nature (MEGAN) (Guenther et al., 2006).

2.2 Numerical experiments

To quantify the impacts of API and ARF on O₃, three case simulations have been conducted: (1) BASE – the base simulation coupled with the interactions between aerosol and radiation, which includes both impacts of API and ARF; (2) NOAPI – the same as the BASE case, but the impact of API is turned off (aerosol optical properties are set to zero in the photolysis module), following Wu et al. (2020); (3) NOALL – both the impacts of API and ARF are turned off (removing the mass of aerosol species when calculating aerosol optical properties in the optical module), following Qiu et al. (2017). The differences between BASE and NOAPI (i.e., BASE minus NOAPI) represent the impacts of API. The contributions from ARF can be obtained by comparing NOAPI and NOALL (i.e., NOAPI minus NOALL). The combined effects of API and ARF on O₃ concentrations can be quantitatively evaluated by the differences between BASE and NOALL (i.e., BASE minus NOALL).

All the experiments in Episode1, Episode2 and Episode3 are conducted from 26 July to 3 August 2014, 6-13 July 2015 and 3-11 June 2016, respectively, with the first 40 hours as the model spin-up in each case. Simulation results from the BASE cases of the three episodes are used to evaluate the model performance.

2.3 Observational data

Simulation results are compared with meteorological and chemical measurements. The surface-layer meteorological data (2 m temperature (T₂), 2 m relative humidity (RH₂), and 10 m wind speed (WS₁₀)) with the temporal resolution of 3 h at ten stations (Table S1) are obtained from NOAA's National Climatic Data Center (<https://gis.ncdc.noaa.gov/maps/ncei/cdo/hourly>). The radiosonde data of temperature at 08:00 and 20:00 LST in Beijing (39.93 °N, 116.28 °E) are provided by the University of Wyoming (<http://weather.uwyo.edu/>). Observed hourly concentrations of PM_{2.5} and O₃ at thirty-two sites (Table S2) in North China are collected from the China National Environmental Monitoring Center (CNEMC). The photolysis rate of nitrogen dioxide (J[NO₂]) measured at the Peking University site (39.99 °N, 116.31 °E) is also used to evaluate the model performance. More details

about the measurement technique of $J[\text{NO}_2]$ can be found in Wang et al. (2019). The aerosol optical depth (AOD) at Beijing site (39.98°N, 116.38°E) is provided by AERONET (level 2.0, <http://aeronet.gsfc.nasa.gov/>). The AOD at 675 nm and 440 nm are used to derive the AOD at 550 nm to compare with the simulated ones.

2.4 Integrated process rate analysis

Integrated process rate (IPR) analysis has been widely used to quantify the contributions of different processes to O_3 variations (Goncalves et al., 2009; Gao et al., 2016b; Tang et al., 2017; Gao et al., 2018). In this study, four physical/chemical processes are considered, including vertical mixing (VMIX), net chemical production (CHEM), horizontal advection (ADVH), and vertical advection (ADVZ). VMIX is initiated by turbulent process and closely related to PBL development, which influences O_3 vertical gradients. CHEM represents the net O_3 chemical production (chemical production minus chemical consumption). ADVH and ADVZ represent transport by winds (Gao et al., 2016b). In this study, we define ADV as the sum of ADVH and ADVZ.

3 Model evaluation

Reasonable representation of observed meteorological and chemical variables by the WRF-Chem model can provide foundation for evaluating the impacts of aerosols on surface-layer ozone concentrations. The model results presented in this section are taken from the BASE cases in the three episodes. The concentrations of air pollutants are averaged over the thirty-two observation sites in Beijing, Tianjin and Baoding. To ensure the data quality, the mean value for each time is calculated only when concentrations are available at more than sixteen sites, as did in Li et al. (2019a).

3.1 Chemical simulations

Figure 2 shows the temporal variations of observed and simulated $\text{PM}_{2.5}$ and O_3 concentrations over North China for the three episodes. As shown in Fig. 2, the temporal variations of observed $\text{PM}_{2.5}$ can be well performed by the model with correlation coefficients (R) of 0.66, 0.56 and 0.73 and normalized mean bias (NMB)

of -19.2%, -3.9% and 30.4% during Episode1, Episode2 and Episode3, respectively. The model also tracks well the diurnal variation of O_3 over the North China, with R of 0.86, 0.91 and 0.86 and NMB of -12.0%, 0.4% and 1.6% for Episode1, Episode2 and Episode3, respectively.

Figure S1 shows the correlation between observed and simulated AOD at 550 nm in Beijing. In the WRF-Chem model, the AOD at 550 nm are calculated by using the values at 400 and 600 nm according to the Angstrom exponent. Analyzing Fig. S1, the model can reproduce the observed AOD with R of 0.7 and NMB of 7.9%.

3.2 Meteorological simulations

Figure 3 shows the time series of observed and simulated T_2 , RH_2 , WS_{10} and $J[NO_2]$ during the three episodes. The observed T_2 , RH_2 , WS_{10} are averaged over the ten meteorological observation stations, and the $J[NO_2]$ are measured at Peking University. Most of the monitored $J[NO_2]$ in Episode3 are unavailable, so the comparison of $J[NO_2]$ in Episode3 is not shown. Generally, the model can depict the temporal variations of T_2 fairly well with R of 0.98 and the mean bias (MB) of -1.9~0.9 °C. For RH_2 , the R and MB are 0.91~0.97 and -4.0%~1.9%, respectively. Although WRF-Chem model overestimates WS_{10} with the MB of 0.6~0.9 m s⁻¹, the R for WS_{10} is 0.70~0.89 and the root-mean-square error (RMSE) is 0.9~1.5 m s⁻¹, which is smaller than the threshold of model performance criteria (2 m s⁻¹) proposed by Emery et al. (2001). The positive bias in wind speed can also be reproduced in other studies (Zhang et al., 2010; Gao et al., 2015; Liao et al., 2015; Qiu et al., 2017). The predicted $J[NO_2]$ agrees well with the observations with R of 0.97~0.98 and NMB of 6.8%~6.9%. We also conduct comparisons of observed and simulated temperature profiles at 08:00 and 20:00 LST in Beijing during the three episodes (Fig. S2). The vertical profiles of observed temperature can be well captured by the model in these three complex air pollution episodes. Generally, the WRF-Chem model can reasonably reproduce the temporal variations of observed meteorological parameters.

4 Results

It is known that co-occurrence of $PM_{2.5}$ and O_3 pollution is frequently observed

nowadays over China (Dai et al., 2021). The complex air pollution characterized by high $\text{PM}_{2.5}$ and O_3 levels has already received widespread attention from both scientists and policy-makers. Therefore, we examine the impacts of aerosol-radiation interactions on O_3 concentrations with a special focus on the complex air pollution areas (CAPAs, Fig. S3) in the three episodes, where the mean simulated daily $\text{PM}_{2.5}$ and MDA8 (maximum daily 8-h average) O_3 concentrations are larger than $75 \mu\text{g m}^{-3}$ and 80 ppb, respectively, based on the National Ambient Air Quality Standards (<http://www.mee.gov.cn>).

4.1 Impacts of aerosol-radiation interactions on meteorology

Figure 4 shows the impacts of aerosol-radiation interactions on shortwave radiation at the surface (BOT_SW), shortwave radiation in the atmosphere (ATM_SW), PBLH, and WS_{10} during the daytime (08:00-17:00 LST) from Episode1 to Episode3. Analyzing the results of the interactions between aerosol and radiation (the combined impacts of API and ARF), BOT_SW is decreased over the entire simulated domain in the three episodes with the decreases of 93.2 W m^{-2} (20.5%), 100.3 W m^{-2} (19.5%) and 92.4 W m^{-2} (19.2%) over CAPAs, respectively. Contrary to the changes in BOT_SW, ATM_SW is increased significantly in the three episodes with the increases of 72.8 W m^{-2} (25.3%), 85.2 W m^{-2} (29.0%) and 73.7 W m^{-2} (26.4%) over CAPAs, respectively. The decreased BOT_SW perturbs the near-surface energy flux, which weakens convection and suppresses the development of PBL (Li et al., 2017b). The mean PBLHs over CAPAs are decreased by 129.0 m (13.0%), 249.0 m (20.9%) and 224.6 m (19.0%), respectively. WS_{10} exhibits overall reductions over CAPAs and is calculated to decrease by 0.12 m s^{-1} (3.6%), 0.05 m s^{-1} (1.6%), and 0.12 m s^{-1} (3.0%) for the three episodes, respectively. We also examine the changed meteorological variables caused by API and ARF respectively. As shown in Fig. S4 and S5, API has little impact on meteorological variables; which means the major contributor to the meteorology variability is ARF.

4.2 Impacts of aerosol-radiation interactions on photolysis

Figure 5 shows the spatial distributions of mean daytime surface-layer $\text{PM}_{2.5}$

concentrations simulated by BASE cases and the changes in $J[\text{NO}_2]$ and $J[\text{O}^1\text{D}]$ due to aerosol-radiation interactions from Episode1 to Episode3. When the combined impacts (API and ARF) are considered, $J[\text{NO}_2]$ and $J[\text{O}^1\text{D}]$ are decreased over the entire domain in the three episodes, and the spatial patterns of changed $J[\text{NO}_2]$ and $J[\text{O}^1\text{D}]$ are similar to that of simulated $\text{PM}_{2.5}$. Analyzing the three simulated episodes, the surface $J[\text{NO}_2]$ averaged over CAPAs are decreased by $1.8 \times 10^{-3} \text{ s}^{-1}$ (40.5%), $2.0 \times 10^{-3} \text{ s}^{-1}$ (36.8%) and $1.8 \times 10^{-3} \text{ s}^{-1}$ (36.0%), respectively. The decreased surface $J[\text{O}^1\text{D}]$ over CAPAs are $6.1 \times 10^{-6} \text{ s}^{-1}$ (48.8%), $6.3 \times 10^{-6} \text{ s}^{-1}$ (41.4%) and $5.7 \times 10^{-6} \text{ s}^{-1}$ (44.6%), respectively. Figure S6 exhibits the impacts of API and ARF on surface $J[\text{NO}_2]$ and $J[\text{O}^1\text{D}]$. Conclusions can be summarized that $J[\text{NO}_2]$ and $J[\text{O}^1\text{D}]$ are significantly modified by API and little affected by ARF.

4.3 Impacts of aerosol-radiation interactions on O_3

Figure 6 shows the changes in surface-layer O_3 due to API, ARF, and the combined effects (denoted as ALL) from Episode1 to Episode3. As shown in Fig. 6(a1-a3), API alone leads to overall surface O_3 decreases over the entire domain with average reductions of 8.5 ppb (10.1%), 9.0 ppb (10.6%) and 8.3 ppb (10.4%) over CAPAs in the three episodes, respectively. The changes can be explained by the substantially diminished UV radiation due to aerosol loading, which significantly weakens the efficiency of photochemical reactions and restrains O_3 formation. However, the decreased surface O_3 concentrations due to ARF are only 2.9 ppb (3.1%, Fig. 6(b1)), 1.0 ppb (1.2%, Fig. 6(b2)) and 1.0 ppb (1.1%, Fig. 6(b3)) for the three episodes, which indicates that API is the dominant way for O_3 reduction related to aerosol-radiation interactions. Fig. 6(c1-c3) presents the combined effects of API and ARF. Generally, aerosol-radiation interactions decrease the surface O_3 concentrations by 11.4 ppb (13.5%), 10.0 ppb (11.9%) and 9.3 ppb (11.6%) averaged over CAPAs in the three episodes, respectively.

4.4 Influencing mechanism of aerosol-radiation interactions on O_3

Figure 7a shows mean results of the three episodes (Episode1, Episode2 and Episode3) in diurnal variations of simulated daytime surface-layer O_3 concentrations

from BASE, NOAPI and NOALL cases averaged over CAPAs. All the experiments (BASE, NOAPI and NOALL) present O₃ increases from 08:00 LST. It is shown that the simulated O₃ concentrations in BASE case increase more slowly than that in NOAPI and NOALL cases. To explain the underlying mechanisms of API and ARF impacts on O₃, we quantify the variations in contributions of different processes (ADV, CHEM, and VMIX) to O₃ by using the IPR analysis.

Figure 7b shows hourly surface O₃ changes induced by each physical/chemical process (i.e., ADV, CHEM, and VMIX) in BASE case averaged from Episode1 to Episode3. The significant positive contribution to the hourly variation in O₃ is contributed by VMIX, and the contribution reaches the maximum at about 09:00 LST. The CHEM process makes negative contributions at around 09:00 and 16:00 LST, which means that the chemical consumption of O₃ is stronger than the chemical production. At noon, the net chemical contribution turns to be positive due to stronger solar UV radiation. The contribution from all the processes (NET, the sum of VMIX, CHEM, and ADV) to O₃ variation is peaked at the noon and then becomes weakened. After sunset (17:00 LST), the NET contribution turns to be negative over CAPAs, leading to O₃ decrease.

Figure 7c shows the changes in hourly process contributions caused by API averaged from Episode1 to Episode3. The chemical production of O₃ is suppressed significantly due to aerosol impacts on photolysis rates. The weakened O₃ chemical production decreases the contribution from CHEM, and results in a negative value of CHEM_DIF (-3.2 ppb h⁻¹). In contrast to CHEM_DIF, the contribution from changed VMIX (VMIX_DIF) to O₃ concentration due to API is always positive, and the mean value is +3.0 ppb h⁻¹. The impact of API on ADV process is relatively small (-0.26 ppb h⁻¹). NET_DIF, namely the sum of VMIX_DIF, CHEM_DIF and ADV_DIF, indicates the differences in hourly O₃ changes caused by API. As shown in Fig. 7c, NET_DIF is almost negative during the daytime over CAPAs with the mean value of -0.46 ppb h⁻¹. This is because the decreases in CHEM and ADV are larger than the increases in VMIX caused by API; the O₃ decrease is mainly attributed to the significantly decreased contribution from CHEM. The maximum difference in O₃

between BASE and NOAPI appears at 11:00 LST with a value of -11.1 ppb (Fig. 7a).

Figure 7d shows the impacts of ARF on each physical/chemical process contribution to the hourly O₃ variation averaged from Episode1 to Episode3. At 08:00 LST, the change in VMIX due to ARF is large with a value of -3.5 ppb h⁻¹, resulting in a net negative variation with all processes considered. The decrease in O₃ reaches the maximum with the value of 5.2 ppb at around 08:00 LST over CAPAs (Fig. 7a). During 09:00 to 16:00 LST, the positive VMIX_DIF (mean value of +0.20 ppb h⁻¹) or the positive CHEM_DIF (mean value of +0.55 ppb h⁻¹) is the major process to positive NET_DIF.

When both impacts of API and ARF are considered, the variation pattern of the difference in hourly process contribution shown in Fig. 7e is similar to that in Fig. 7c, which indicates that API is the dominant factor to surface-layer O₃ reduction.

Figure 8 presents the vertical profiles of simulated daytime O₃ concentrations in three cases (BASE, NOAPI, and NOALL), and the differences in contributions from each physical/chemical process to hourly O₃ variations caused by API, ARF and the combined effects averaged over CAPAs from Episode1 to Episode3. As shown in Fig. 8a, the O₃ concentration is lower in BASE than that in other two scenarios (NOAPI and NOALL), especially at the lower 12 levels (below 863.0 m), owing to the impacts of aerosols (API and/or ARF).

The changes in each process contribution caused by API are presented in Fig. 8b. The contribution from CHEM_DIF is -2.0 ppb h⁻¹ for the first seven layers (from 27.6 to 342.8 m). Conversely, the contribution from VMIX_DIF shows a positive value under the 342.8 m (between the first layer to the seventh layer) with the mean value of +1.7 ppb h⁻¹. The positive variation in VMIX due to API may be associated with the different vertical gradient of O₃ between BASE and NOAPI. The contributions of changed advections (ADVH_DIF and ADVZ_DIF) are relatively small, with mean values of +0.07 and -0.21 ppb h⁻¹ below the first seven layers, which may result from small impact of API on wind field (Fig. S5(a4-c4)). The net difference is a negative value (-0.44 ppb h⁻¹); API leads to O₃ reduction not only nearly surface but also aloft.

Figure 8c shows the differences in O₃ budget due to ARF. When the ARF is

considered, the vertical turbulence is weakened and the development of PBL is inhibited, which makes VMIX_DIF negative at the lower seven layers (below the 342.8 m) with a mean value of -0.64 ppb h^{-1} , but the variation in CHEM caused by ARF is positive with a mean value of $+0.72 \text{ ppb h}^{-1}$. The enhanced O_3 precursors due to ARF can promote the chemical production of O_3 (Tie et al., 2009; Gao et al., 2018). The changes of ADVZ and ADVH (ADVZ_DIF and ADVH_DIF) caused by ARF are associated with the variations in wind field. When ARF is considered, the horizontal wind speed is decreased (Fig. S7(a)), which makes ADVH_DIF positive at the lower twelve layers with a mean value of $+0.25 \text{ ppb h}^{-1}$. However, ADVZ_DIF is negative at these layers with a mean value of -0.27 ppb h^{-1} because aerosol radiative effects decrease the transport of O_3 from the upper to lower layers (Fig. S7(b)).

In Fig. 8d, the pattern and magnitude of the differences in process contributions between BASE and NOALL are similar to those caused by API, indicating the dominate contributor of API on O_3 changes. The impacts of API on O_3 both near the surface and aloft are greater than those of ARF.

Figure S8 and S9 detailed show the influencing mechanism of aerosol-radiation interactions on O_3 in each episode. Similar variation characteristics can be found among the three episodes as the mean situation discussed above, with the larger impacts of API on O_3 both near the surface and aloft than those of ARF, indicating the major contributor of API on O_3 reduction related with aerosol-radiation interactions.

5 Conclusions and Discussions

In this study, the fully coupled regional chemistry transport model WRF-Chem is applied to investigate the impacts of aerosol-radiation interactions, including the impacts of aerosol-photolysis interaction (API) and the impacts of aerosol-radiation feedback (ARF), on O_3 during summertime complex air pollution episodes during 28 July to 3 August 2014 (Episode1), 8-13 July 2015 (Episode2) and 5-11 June 2016 (Episode3). Three sensitivity experiments are designed to quantify the respective and combined impacts from API and ARF. Generally, the spatiotemporal distributions of observed pollutant concentrations and meteorological parameters can be captured

fairly well by the model with correlation coefficients of 0.56~0.91 for pollutant concentrations and 0.70~0.98 for meteorological parameters.

Sensitivity experiments show that aerosol-radiation interactions decrease BOT_SW, WS₁₀, PBLH, J[NO₂], and J[O¹D] by 92.4~100.3 W m⁻², 0.05~0.12 m s⁻¹, 129.0~249.0 m, 1.8×10^{-3} ~ 2.0×10^{-3} s⁻¹, and 5.7×10^{-6} ~ 6.3×10^{-6} s⁻¹ over CAPAs, and increase ATM_SW by 72.8~85.2 W m⁻². The changed meteorological variables and weakened photochemistry reaction further reduce surface-layer O₃ concentrations by up to 9.3~11.4 ppb, with API and ARF contributing 74.6%~90.0% and 10.0%~25.4%, respectively.

We further examine the influencing mechanism of aerosol-radiation interactions on O₃ by using integrated process rate analysis. API can directly affect O₃ by reducing the photochemistry reactions within the lower several hundred meters and therefore amplify the O₃ vertical gradient, which promotes the vertical mixing of O₃. The reduced photochemistry reactions of O₃ weaken the chemical contribution and reduce surface O₃ concentrations, even though the enhanced vertical mixing can partly counteract the reduction. ARF affects O₃ concentrations indirectly through the changed meteorological variables, e.g., the decreased PBLH. The suppressed PBL can weaken the vertical mixing of O₃ by turbulence. Generally, the impacts of API on O₃ both near the surface and aloft are greater than those of ARF, indicating the dominant role of API on O₃ reduction related with aerosol-radiation interactions.

This study provides a detailed understanding of aerosol impacts on O₃ through aerosol-radiation interactions (including both API and ARF). The results imply that future PM_{2.5} reductions will lead to O₃ increases due to weakened aerosol-radiation interactions. A recent study emphasized the need for controlling VOCs emissions to mitigate O₃ pollution (Li et al., 2019b). Therefore, tighter controls of O₃ precursors (especially VOCs emissions) are needed to counteract future O₃ increases caused by weakened aerosol-radiation interactions, and the contributions of different mitigation strategies with the impacts of aerosol-radiation interactions to O₃ air quality will be discussed detailedly in our future work.

There are some limitations to this work. The uncertainty of the lack of secondary

organic aerosols (SOA), and the missing mechanisms of some heterogeneous reactions may result in large uncertainties in the final simulation results. Gao et al. (2017) added some SOA formation mechanisms into the MOSAIC module by using the volatility basis set (VBS) in WRF-Chem and found that the surface PM_{2.5} concentrations in urban Beijing were reduced by 1.9 $\mu\text{g m}^{-3}$ due to the weakened ARF effect during Asia-Pacific Economic Cooperation (APEC). Similar magnitude can also be found in Zhou et al. (2019) (-1.8 $\mu\text{g m}^{-3}$) who did not consider the impacts of SOA in WRF-Chem when analyzing the impacts of weakened ARF on PM_{2.5} during APEC. Therefore, more work should be conducted to explore the impacts of ARF on PM_{2.5} and O₃ concentrations under consideration of SOA in future.

Data availability

The observed hourly surface concentrations of air pollutants are derived from the China National Environmental Monitoring Center (<http://www.cnemc.cn>). The observed surface meteorological data are obtained from NOAA's National Climatic Data Center (<https://gis.ncdc.noaa.gov/maps/ncei/cdo/hourly>). The radiosonde data are provided by the University of Wyoming (<http://weather.uwyo.edu/>). The photolysis rates of nitrogen dioxide in Beijing are provided by Xin Li (li_xin@pku.edu.cn). The aerosol optical depth in Beijing is obtained from the AERONET level 2.0 data collection (<http://aeronet.gsfc.nasa.gov/>). The simulation results can be accessed by contacting Lei Chen (chenlei@nuist.edu.cn) and Hong Liao (hongliao@nuist.edu.cn).

Author contributions

HY, LC, and HL conceived the study and designed the experiments. HY and LC performed the simulations and carried out the data analysis. JZ, WW, and XL provided useful comments on the paper. HY prepared the paper with contributions from all co-authors.

Competing interests

The authors declare that they have no competing interests.

Acknowledgements

This work is supported by the National Key R&D Program of China (2019YFA0606804), the National Natural Science Foundation of China (42007195), the Meteorological Soft Science Program of China Meteorological Administration (2021ZZXM46), and the Postgraduate Research and Practice Innovation Program of Jiangsu Province (KYCX21_1014). We acknowledge the High Performance Computing Center of Nanjing University of Information Science & Technology for

431 their support of this work.

Reference

- Albrecht, B. A.: Aerosols, cloud microphysics, and fractional cloudiness, *Science*, 245, 1227–1230, 1989.
- Chen, F. and Dudhia, J.: Coupling an Advanced Land Surface – Hydrology Model with the Penn State – NCAR MM5 Modeling System. Part I: Model Implementation and Sensitivity, *Mon. Weather Rev.*, 129(4), 569–585, 2001.
- Chen, L., Zhu, J., Liao, H., Gao, Y., Qiu, Y., Zhang, M., Liu, Z., Li, N., and Wang, Y.: Assessing the formation and evolution mechanisms of severe haze pollution in the Beijing–Tianjin–Hebei region using process analysis, *Atmos. Chem. Phys.*, 19, 10845–10864, <https://doi.org/10.5194/acp-19-10845-2019>, 2019.
- Dai, H., Zhu, J., Liao, H., Li, J., Liang, M., Yang, Y., and Yue, X.: Co-occurrence of ozone and PM_{2.5} pollution in the Yangtze River Delta over 2013–2019: Spatiotemporal distribution and meteorological conditions, *Atmos. Res.*, 249, 105363, 2021.
- Dickerson, R. R., Kondragunta, S., Stenchikov, G., Civerolo, K. L., Doddridge, B. G., and Holben, B. N.: The impact of aerosols on solar ultraviolet radiation and photochemical smog, *Science*, 278, 827–830, 10.1126/science.278.5339.827, 1997.
- Emery, C., Tai, E., and Yarwood, G.: Enhanced meteorological modeling and performance evaluation for two Texas ozone episodes, in: Prepared for the Texas Natural Resource Conservation Commission, ENVIRON International Corporation, Novato, CA, USA, 2001.
- Emmons, L. K., Walters, S., Hess, P. G., Lamarque, J.-F., Pfister, G. G., Fillmore, D., Granier, C., Guenther, A., Kinnison, D., Laepple, T., Orlando, J., Tie, X., Tyndall, G., Wiedinmyer, C., Baughcum, S. L., and Kloster, S.: Description and evaluation of the Model for Ozone and Related chemical Tracers, version 4 (MOZART-4), *Geosci. Model Dev.*, 3, 43–67, doi:10.5194/gmd-3-43-2010, 2010.
- Foken, T.: 50 years of the Monin-Obukhov similarity theory, *Bound.-Layer Meteor.*, 119, 431–437, 2006.
- Gao, J., Li, Y., Zhu, B., Hu, B., Wang, L., and Bao, F.: What have we missed when

studying the impact of aerosols on surface ozone via changing photolysis rates?,
Atmos. Chem. Phys., 20, 10831–10844, [https://doi.org/10.5194/acp-20-10831-](https://doi.org/10.5194/acp-20-10831-2020)
2020, 2020.

Gao, J. H., Zhu, B., Xiao, H., Kang, H. Q., Pan, C., Wang, D. D., and Wang, H. L.:
Effects of black carbon and boundary layer interaction on surface ozone in
Nanjing, China, Atmos. Chem. Phys., 18, 7081–7094, [https://doi.org/10.5194/acp-](https://doi.org/10.5194/acp-18-7081-2018)
18-7081-2018, 2018.

Gao, M., Carmichael, G. R., Wang, Y., Saide, P. E., Yu, M., Xin, J., Liu, Z., and
Wang, Z.: Modeling study of the 2010 regional haze event in the North China Plain,
Atmos. Chem. Phys., 16, 1673–1691, [doi:10.5194/acp-16-1673-2016](https://doi.org/10.5194/acp-16-1673-2016), 2016a.

Gao, J., Zhu, B., Xiao, H., Kang, H., Hou, X., and Shao, P.: A case study of surface
ozone source apportionment during a high concentration episode, under frequent
shifting wind conditions over the Yangtze River Delta, China, Sci. Total Environ.,
544, 853, <https://doi.org/10.1016/j.scitotenv.2015.12.039>, 2016b.

Gao, M., Liu, Z., Wang, Y., Lu, X., Ji, D. and Wang, L.: Distinguishing the roles of
meteorology, emission control measures, regional transport, and co-benefits of
reduced aerosol feedbacks in “APEC” Blue, Atmos. Environ., 167, 476–486, [doi:10.1016/j.atmosenv.2017.08.054](https://doi.org/10.1016/j.atmosenv.2017.08.054), 2017.

Gao, Y., Zhang, M., Liu, Z., Wang, L., Wang, P., Xia, X., Tao, M., and Zhu, L.:
Modeling the feedback between aerosol and meteorological variables in the
atmospheric boundary layer during a severe fog–haze event over the North China
Plain, Atmos. Chem. Phys., 15, 4279–4295, [doi:10.5194/acp-15-4279-2015](https://doi.org/10.5194/acp-15-4279-2015), 2015.

Goncalves, M., Jimenez-Guerrero, P., Baldasano, J.M.: Contribution of atmospheric
processes affecting the dynamics of air pollution in South-Western Europe during a
typical summertime photochemical episode, Atmos. Chem. Phys., 9, 849 – 864,
[doi:10.5194/acp-9-849-2009](https://doi.org/10.5194/acp-9-849-2009), 2009.

Grell, G. A., Peckham, S. E., Schmitz, R., McKeen, S. A., Frost, G., Skamarock, K.,
and Eder, B.: Fully coupled “online” chemistry within the WRF model, Atmos.
Environ., 39, 6957–6975, 2005.

Guenther, A., Karl, T., Harley, P., Wiedinmyer, C., Palmer, P. I., and Geron, C.:

Estimates of global terrestrial isoprene emissions using MEGAN (Model of Emissions of Gases and Aerosols from Nature), *Atmos. Chem. Phys.*, 6, 3181–3210, doi:10.5194/acp-6-3181-2006, 2006.

Hansen, J., Sato, M., and Ruedy, R.: Radiative forcing and climate response, *J. Geophys. Res.*, 102, 6831–6864, 1997.

Haywood, J. and Boucher, O.: Estimates of the direct and indirect radiative forcing due to tropospheric aerosols: A review, *Rev. Geophys.*, 38, 513–543, 2000.

Hong, S.-Y., Noh, Y., and Dudhia, J.: A New Vertical Diffusion Package with an Explicit Treatment of Entrainment Processes, *Mon. Weather Rev.*, 134, 2318–2341, 2006.

Iacono, M. J., Delamere, J. S., Mlawer, E. J., Shephard, M. W., Clough, S. A., and Collins, W. D.: Radiative forcing by long-lived greenhouse gases: Calculations with the AER radiative transfer models, *J. Geophys. Res.*, 113, D13103, doi:10.1029/2008JD009944, 2008.

Li, G., Bei, N., Tie, X., and Molina, L. T.: Aerosol effects on the photochemistry in Mexico City during MCMA-2006/MILAGRO campaign, *Atmos Chem Phys*, 11, 5169–5182, 10.5194/acp-11-5169-2011, 2011.

Li, J. D., Liao, H., Hu, J. L., Li, N.: Severe particulate pollution days in China during 2013–2018 and the associated typical weather patterns in Beijing-Tianjin-Hebei and the Yangtze River Delta regions, *Environmental Pollution*, 248, 74–81, 2019a.

Li, K., Jacob, D. J., Liao, H., Zhu, J., Shah, V., Shen, L., Bates, K. H., Zhang, Q., and Zhai, S.: A two-pollutant strategy for improving ozone and particulate air quality in China, *Nat. Geosci.*, 12, 906–910, <https://doi.org/10.1038/s41561-019-0464-x>, 2019b.

Li, M., Zhang, Q., Kurokawa, J.-I., Woo, J.-H., He, K., Lu, Z., Ohara, T., Song, Y., Streets, D. G., Carmichael, G. R., Cheng, Y., Hong, C., Huo, H., Jiang, X., Kang, S., Liu, F., Su, H., and Zheng, B.: MIX: a mosaic Asian anthropogenic emission inventory under the international collaboration framework of the MICS-Asia and HTAP, *Atmos. Chem. Phys.*, 17, 935–963, <https://doi.org/10.5194/acp-17-935-2017>, 2017a.

Li, Z., Guo, J., Ding, A., Liao, H., Liu, J., Sun, Y., Wang, T., Xue, H., Zhang, H., and Zhu, B.: Aerosol and boundary-layer interactions and impact on air quality, *Nat. Sci. Rev.*, 4, 810–833, <https://doi.org/10.1093/nsr/nwx117>, 2017b.

Liao, H., Yung, Y. L., and Seinfeld, J. H.: Effects of aerosols on tropospheric photolysis rates in clear and cloudy atmospheres, *J. Geophys. Res.*, 104, 23697–23707, 1999.

Liao, L., Lou, S. J., Fu, Y., Chang, W. Y., and Liao, H.: Radiative forcing of aerosols and its impact on surface air temperature on the synoptic scale in eastern China [in Chinese], *Chin. J. Atmos. Sci.*, 39, 68–82, doi: 10.3878/j.issn.1006-9895.1402.13302, 2015.

Lin, Y.-L., Farley, R. D., and Orville, H. D.: Bulk parameterization of the snow field in a cloud model, *J. Clim. Appl. Meteorol.*, 22, 1065–1092, 1983.

Liu, Y. and Wang, T.: Worsening urban ozone pollution in China from 2013 to 2017 – Part 1: The complex and varying roles of meteorology, *Atmos. Chem. Phys.*, 20, 6305–6321, <https://doi.org/10.5194/acp-20-6305-2020>, 2020.

Lo, J. C.-F., Yang, Z. L., and Pielke Sr, R. A.: Assessment of three dynamical climate downscaling methods using the Weather Research and Forecasting (WRF) model, *J. Geophys. Res.*, 113, D09112, doi:10.1029/2007jd009216, 2008.

Lohmann, U., and Feichter, J.: Global indirect aerosol effects: A review. *Atmospheric Chemistry and Physics*, 5, 715–737, <https://doi.org/10.5194/acp-5-715-2005>, 2005.

Lou, S., Liao, H., and Zhu, B.: Impacts of aerosols on surface-layer ozone concentrations in China through heterogeneous reactions and changes in photolysis rates, *Atmos. Environ.*, 85, 123–138, 2014.

Miao, Y., Liu, S., Guo, J., Huang, S., Yan, Y., and Lou, M.: Unraveling the relationships between boundary layer height and PM_{2.5} pollution in China based on four-year radiosonde measurements, *Environmental Pollution*, <https://doi.org/10.1016/j.envpol.2018.09.070>, 2018.

Otte, T. L.: The impact of nudging in the meteorological model for retrospective air quality simulations. Part I: Evaluation against national observation networks. *J. Appl. Meteor. Climatol.*, 47, 1853–1867, 2008.

Petäjä, T., Järvi, L., Kerminen, V. M., Ding, A. J., Sun, J. N., Nie, W., Kujansuu, J.,
 Virkkula, A., Yang, X., Fu, C. B., Zilitinkevich, S., and Kulmala, M.: Enhanced air
 pollution via aerosol-boundary layer feedback in China, *Sci. Rep.*, 6, 18998,
 doi:10.1038/srep18998, 2016.

Qiu, Y., Liao, H., Zhang, R., and Hu, J.: Simulated impacts of direct radiative effects
 of scattering and absorbing aerosols on surface layer aerosol concentrations in
 China during a heavily polluted event in February 2014, *J. Geophys. Res. Atmos.*,
 122, 5955–5975, doi:10.1002/2016JD026309, 2017.

Skamarock, W., Klemp, J. B., Dudhia, J., Gill, D. O., Barker, D. M., Duda, M., Huang,
 X. Y., Wang, W., and Powers, J. G.: A description of the advanced research WRF
 version 3, NCAR technical note NCAR/TN/u2013475, 2008.

Tang, G. Q., Zhu, X. W., Xin, J. Y., Hu, B., Song, T., Sun, Y., Zhang, J. Q., Wang, L. L.,
 Cheng, M. T., Chao, N., Kong, L. B., Li, X., and Wang, Y. S.: Modelling study of
 boundary-layer ozone over northern China – Part I: Ozone budget in summer,
Atmos. Res., 187, 128–137, 2017.

Tie, X., Geng, F., Li, P., Gao, W., and Zhao, C.: Measurement and modelling of ozone
 variability in Shanghai, China, *Atmos. Environ.*, 43, 4289–4302, 2009.

Wang, W., Li, X., Shao, M., Hu, M., Zeng, L., Wu, Y., and Tan, T.: The impact of
 aerosols on photolysis frequencies and ozone production in Beijing during the 4-
 year period 2012–2015, *Atmos. Chem. Phys.*, 19, 9413–9429,
<https://doi.org/10.5194/acp19-9413-2019>, 2019.

Wild, O., Zhu, X., and Prather, M. J.: Fast-J: Accurate simulation of in- and below-
 cloud photolysis in tropospheric chemical models, *J. Atmos. Chem.*, 37, 245–282,
 doi:10.1023/A:1006415919030, 2000.

Wu, J., Bei, N., Hu, B., Liu, S., Wang, Y., Shen, Z., Li, X., Liu, L., Wang, R., Liu, Z.,
 Cao, J., Tie, X., Molina, L. T., Li, G.: Aerosol-photolysis interaction reduces
 particulate matter during wintertime haze events, *Proc. Natl. Acad. Sci. USA*, 117,
 9755–9761, 2020.

Xing, J., Wang, J. D., Mathur, R., Wang, S. X., Sarwar, G., Pleim, J., Hogrefe, C.,
 Zhang, Y. Q., Jiang, J. K., Wong, D. and Hao, J. M.: Impacts of aerosol direct

effects on tropospheric ozone through changes in atmospheric dynamics and photolysis rates, *Atmos. Chem. Phys.*, 17, 9869–9883, <https://doi.org/10.5194/acp-17-9869-2017>, 2017.

Zaveri, R. A. and Peters, L. K.: A new lumped structure photochemical mechanism for large-scale applications, *J. Geophys. Res.*, 104, D23, 30387–30415, <https://doi.org/10.1029/1999JD900876>, 1999.

Zaveri, R. A., Easter, R. C., Fast, J. D., and Peters, L. K.: Model for simulating aerosol interactions and chemistry (MOSAIC), *J. Geophys. Res.*, 113, D13204, <https://doi.org/10.1029/2007JD008782>, 2008.

Zhang, X., Zhang, Q., Hong, C. P., Zheng, Y. X., Geng, G. N., Tong, D., Zhang, Y. X., and Zhang, X. Y.: Enhancement of PM_{2.5} concentrations by aerosol-meteorology interactions over China. *Journal of Geophysical Research: Atmospheres*, 123, 1179–1194, <https://doi.org/10.1002/2017JD027524>, 2018.

Zhang, Y., Wen, X.-Y., and Jang, C. J.: Simulating chemistry– aerosol–cloud– radiation–climate feedbacks over the continental US using the online-coupled Weather Research Forecasting Model with chemistry (WRF/Chem), *Atmos. Environ.*, 44, 3568–3582, doi:10.1016/j.atmosenv.2010.05.056, 2010.

Zhao, H.; Zheng, Y., and Li, C. Spatiotemporal distribution of PM_{2.5} and O₃ and their interaction during the summer and winter seasons in Beijing, China. *Sustainability*, 10, 4519, 2018.

Zhou, M., Zhang, L., Chen, D., Gu, Y., Fu, T.-M., Gao, M., Zhao, Y., Lu, X. and Zhao, B.: The impact of aerosol-radiation interactions on the effectiveness of emission control measures, *Environmental Research Letters*, 14(2), 024002, <https://doi.org/10.1088/1748-9326/aaf27d>, 2019.

Zhu, J., Chen, L., Liao, H., and Dang, R.: Correlations between PM_{2.5} and Ozone over China and Associated Underlying Reasons, *Atmosphere*, 352, 1–15, <https://doi.org/10.3390/atmos10070352>, 2019.

Zhu, J., Chen, L., Liao, H., Yang, H., Yang, Y., and Yue, X.: Enhanced PM_{2.5} Decreases and O₃ Increases in China During COVID-19 Lockdown by Aerosol-Radiation Feedback, *Geophys. Res. Lett.*, 48,

611 <https://doi.org/10.1029/2020GL090260>, 2021.

1 **Table 1.** Physical parameterization options used in the simulation.

Options	Schemes
Microphysics scheme	Lin (Purdue) scheme (Lin et al.,1983)
Cumulus scheme	Grell 3D ensemble scheme
Boundary layer scheme	Yonsei University PBL scheme (Hong et al., 2006)
Surface layer scheme	Monin-Obukhov surface scheme (Foken, 2006)
Land-surface scheme	Unified Noah land-surface model (Chen and Dudhia, 2001)
Longwave radiation scheme	RRTMG (Iacono et al., 2008)
Shortwave radiation scheme	RRTMG (Iacono et al., 2008)

2

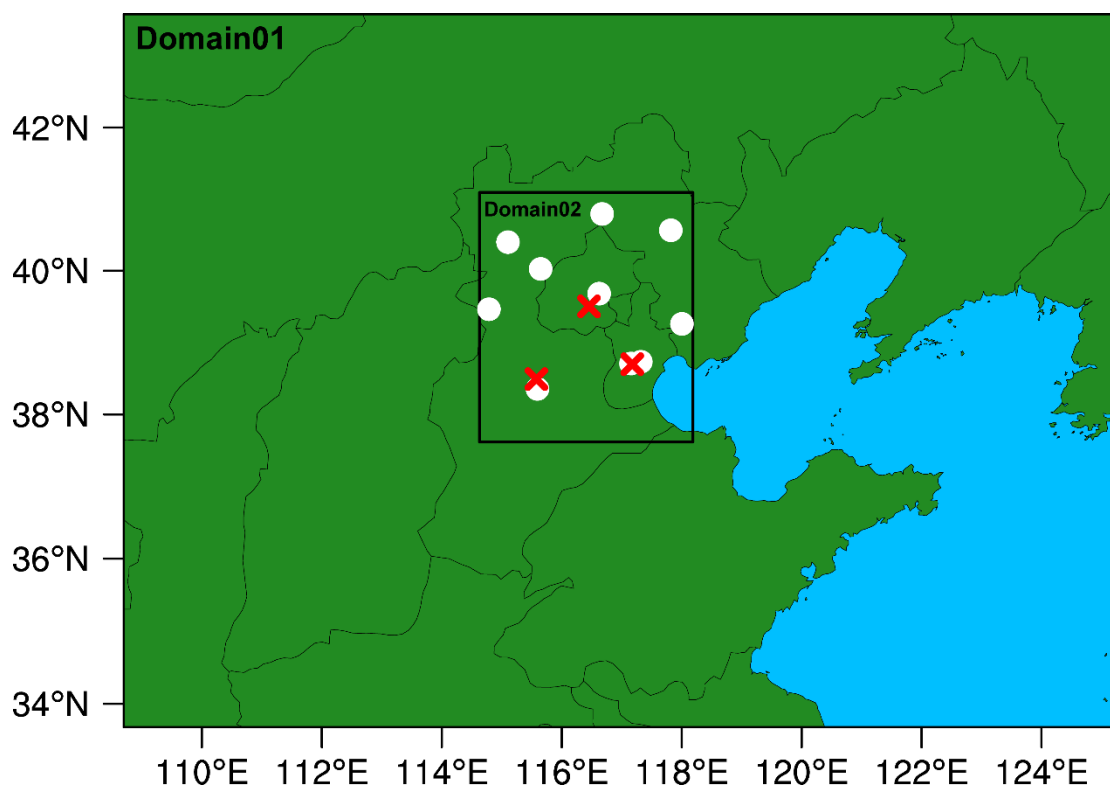


Figure 1. Map of the two WRF-Chem modeling domains with the locations of meteorological (white dots) and environmental (red crosses) observation sites used for model evaluation.

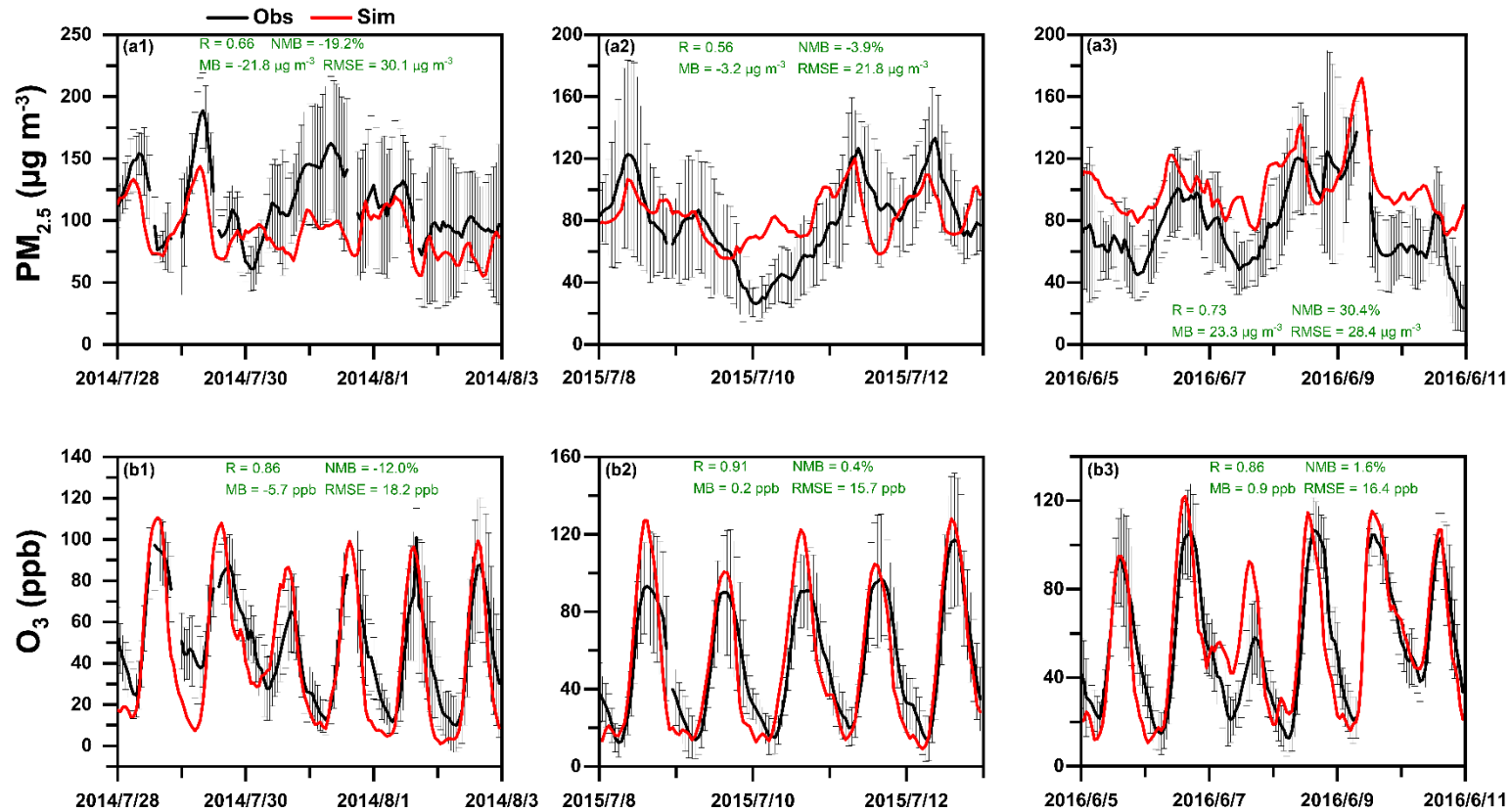


Figure 2. Time series of observed (black) and simulated (red) hourly surface (a) $PM_{2.5}$ and (b) O_3 concentrations averaged over the thirty-two observation sites in Beijing, Tianjin, and Baoding during 28 July to 3 August 2014 (Episode1, a1-b1), 8-13 July 2015 (Episode2, a2-b2) and 5-11 June 2016 (Episode3, a3-b3). The error bars represent the standard deviations. The calculated correlation coefficient (R), mean bias (MB), normalized mean bias (NMB) and root-mean-square error (RMSE) are also shown.

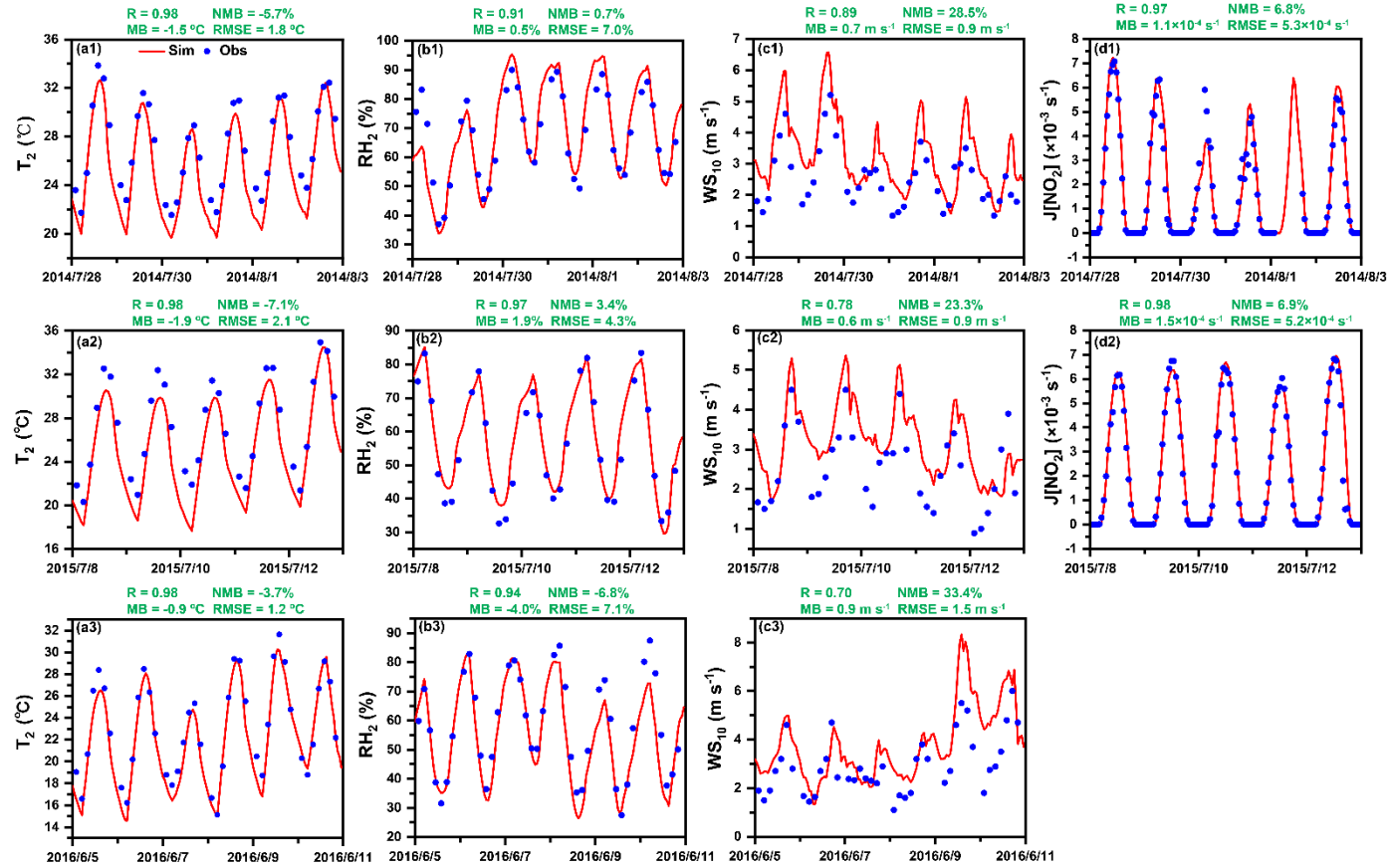


Figure 3. Time series of 3-hourly observed (blue dots) and hourly simulated (red lines) (a) 2-m temperature (T_2), (b) 2-m relative humidity (RH_2), (c) wind speed at 10 m (WS_{10}) averaged over ten meteorological observation stations, and (d) surface photolysis rate of NO_2 ($J[NO_2]$) during 28 July to 3 August 2014 (Episode1, a1-d1), 8-13 July 2015 (Episode2, a2-d2) and 5-11 June 2016 (Episode3, a3-c3). The calculated correlation coefficient (R), mean bias (MB), normalized mean bias (NMB) and root-mean-square error (RMSE) are also shown.

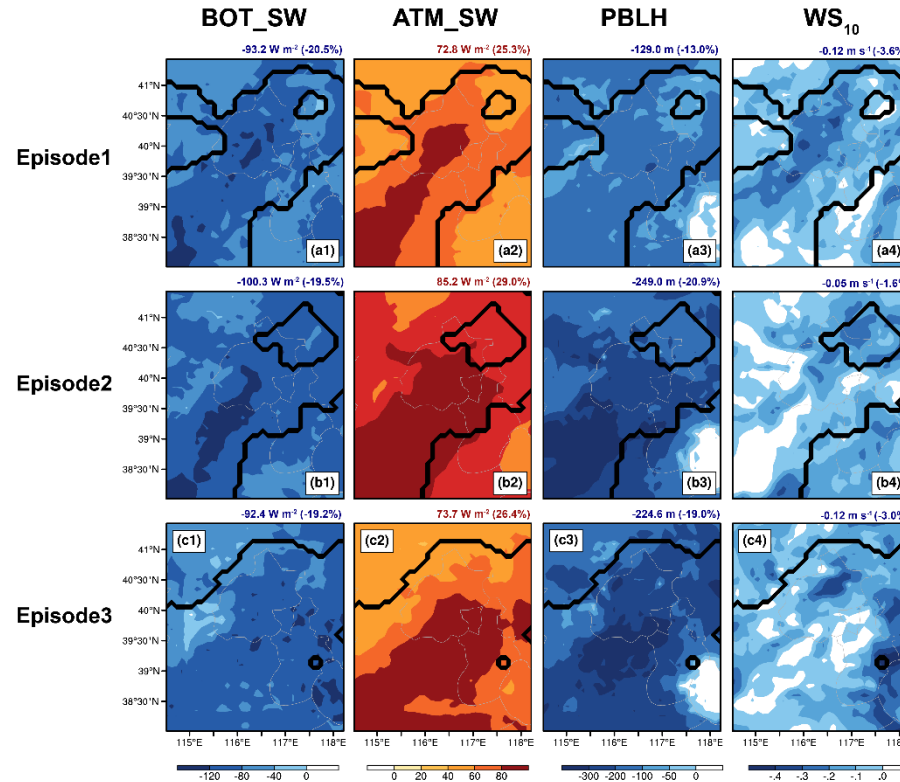


Figure 4. The impacts of aerosol-radiation interactions on shortwave radiation at the surface (BOT_SW), shortwave radiation in the atmosphere (ATM_SW), PBL height (PBLH), and 10-m wind speed (WS₁₀) in the daytime (08:00-17:00 LST) during 28 July to 3 August 2014 (Episode1), 8-13 July 2015 (Episode2) and 5-11 June 2016 (Episode3). The regions sandwiched between two black lines are defined as the complex air pollution areas (CAPAs) where the mean daily PM_{2.5} and MDA8 O₃ concentrations in BASE case are larger than 75 $\mu\text{g m}^{-3}$ and 80 ppb. The calculated changes (percentage changes) averaged over CAPAs are also shown at the top of each panel.

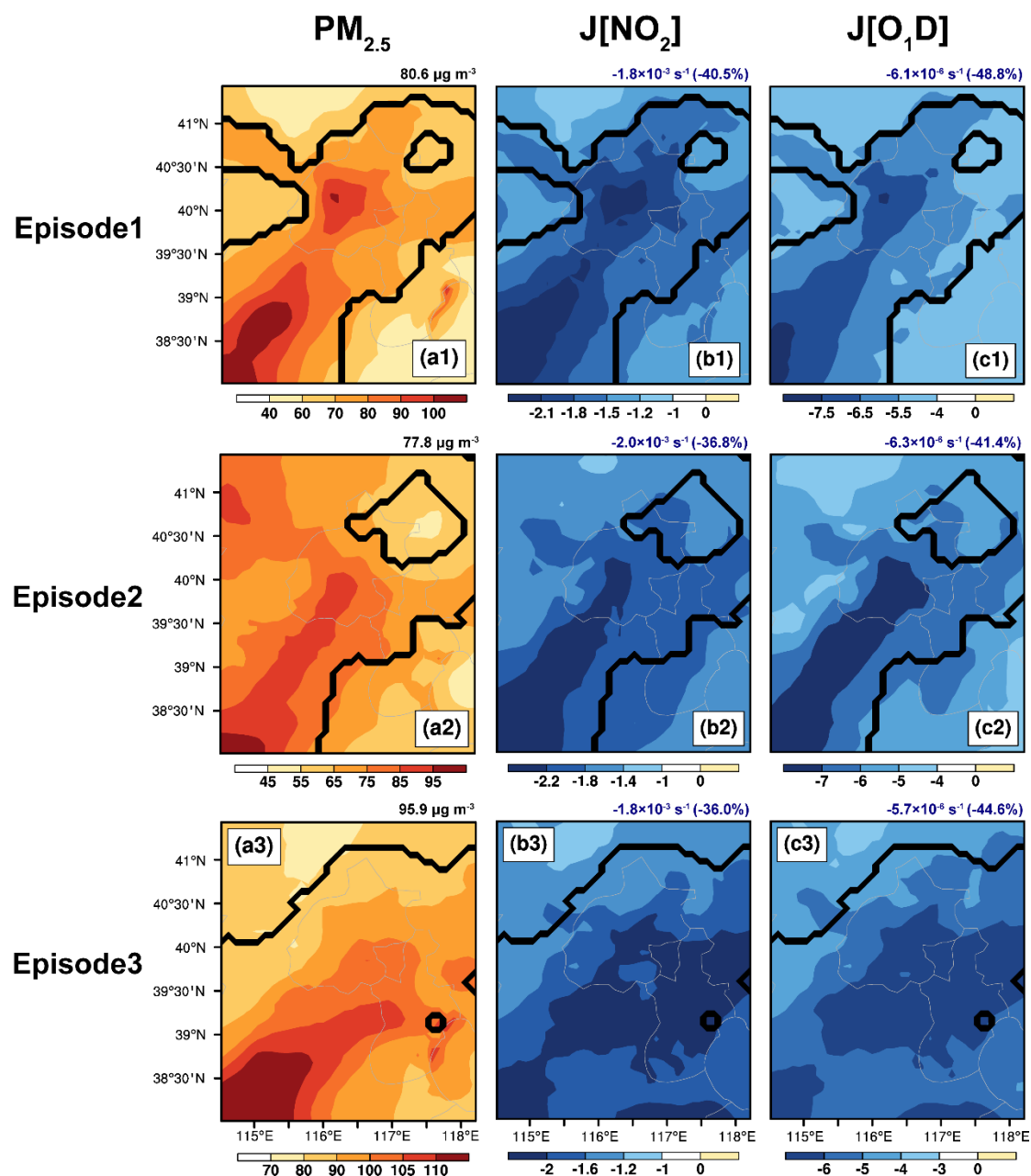


Figure 5. Spatial distributions of (a) simulated surface-layer PM_{2.5} concentrations in BASE cases, and the changes in surface (b) J[NO₂] and (c) J[O¹D] due to aerosol-radiation interactions in the daytime (08:00-17:00 LST) during 28 July to 3 August 2014 (Episode1), 8-13 July 2015 (Episode2) and 5-11 June 2016 (Episode3). The calculated values (percentage changes) averaged over CAPAs are also shown at the top of each panel.

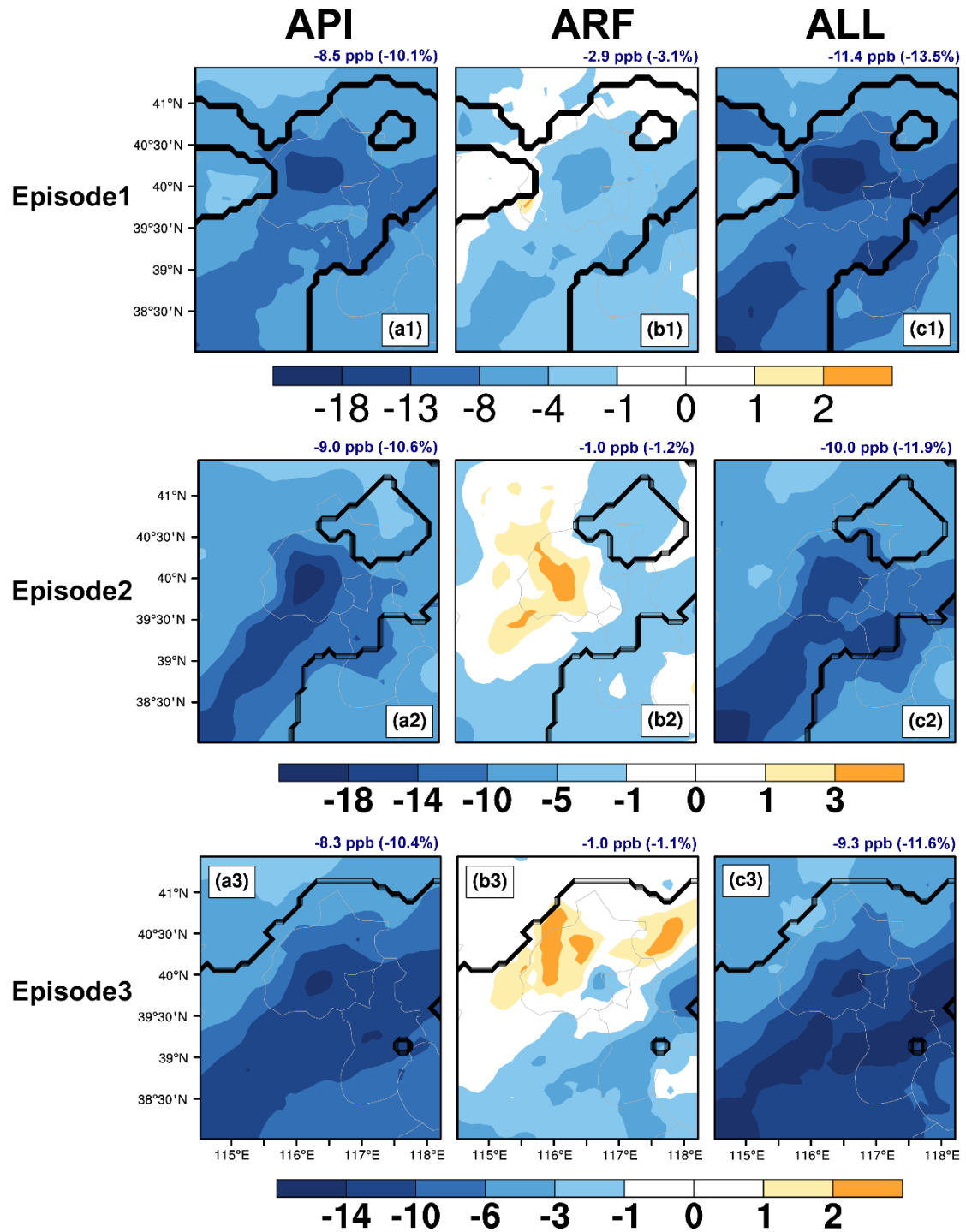
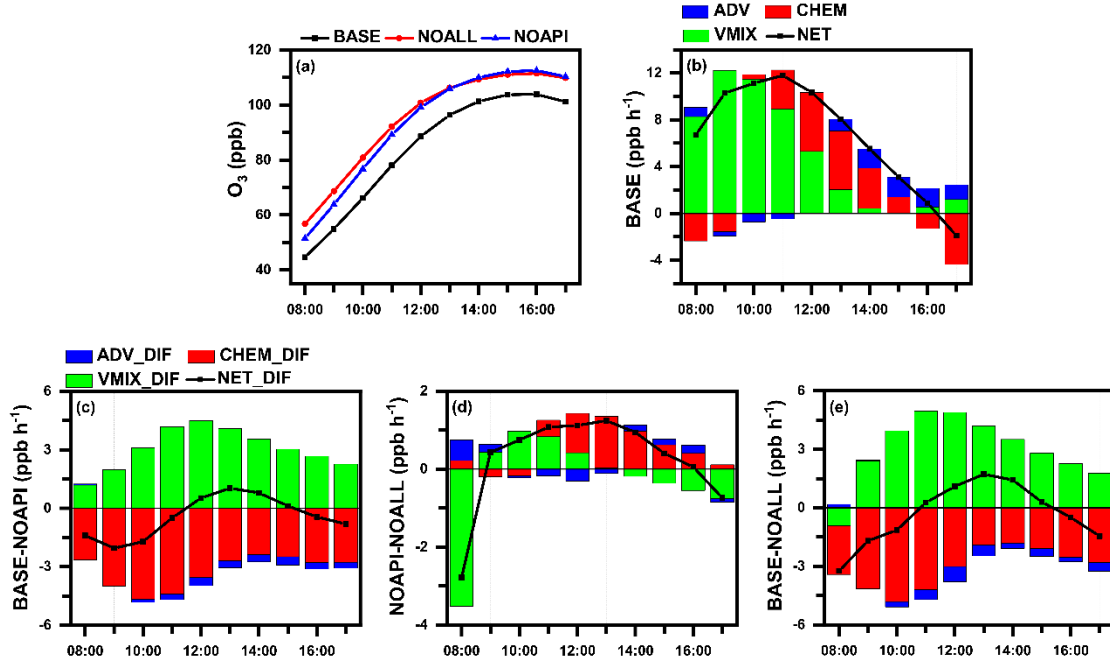


Figure 6. The changes in surface-layer ozone due to (a) aerosol-photolysis interaction (API), (b) aerosol-radiation feedback (ARF), and (c) the combined effects (ALL, defined as API+ARF) in the daytime (08:00-17:00 LST) during 28 July to 3 August 2014 (Episode1), 8-13 July 2015 (Episode2) and 5-11 June 2016 (Episode3). The calculated mean changes (percentage changes) averaged over CAPAs are also shown at the top of each panel.

1



2

3 **Figure 7.** Temporal evolution characteristics of aerosol-radiation interactions on O₃
4 averaged over the three episodes. (a) Diurnal variations of simulated surface O₃
5 concentrations in BASE (black dotted line), NOAPI (blue dotted line), and NOALL
6 (red dotted line) cases over CAPAs. (b) The hourly surface O₃ changes induced by
7 each physical/chemical process using the IPR analysis method in BASE case. (c-e)
8 Changes in hourly surface O₃ process contributions caused by API (BASE minus
9 NOAPI), ARF (NOAPI minus NOALL), and ALL (BASE minus NOALL) over
10 CAPAs during the daytime (08:00-17:00 LST). The black lines with squares denote
11 the net contribution of all processes (NET, defined as VMIX+CHEM+ADV).
12 Differences of each process contribution are denoted as VMIX_DIF, CHEM_DIF,
13 ADV_DIF, and NET_DIF.

14

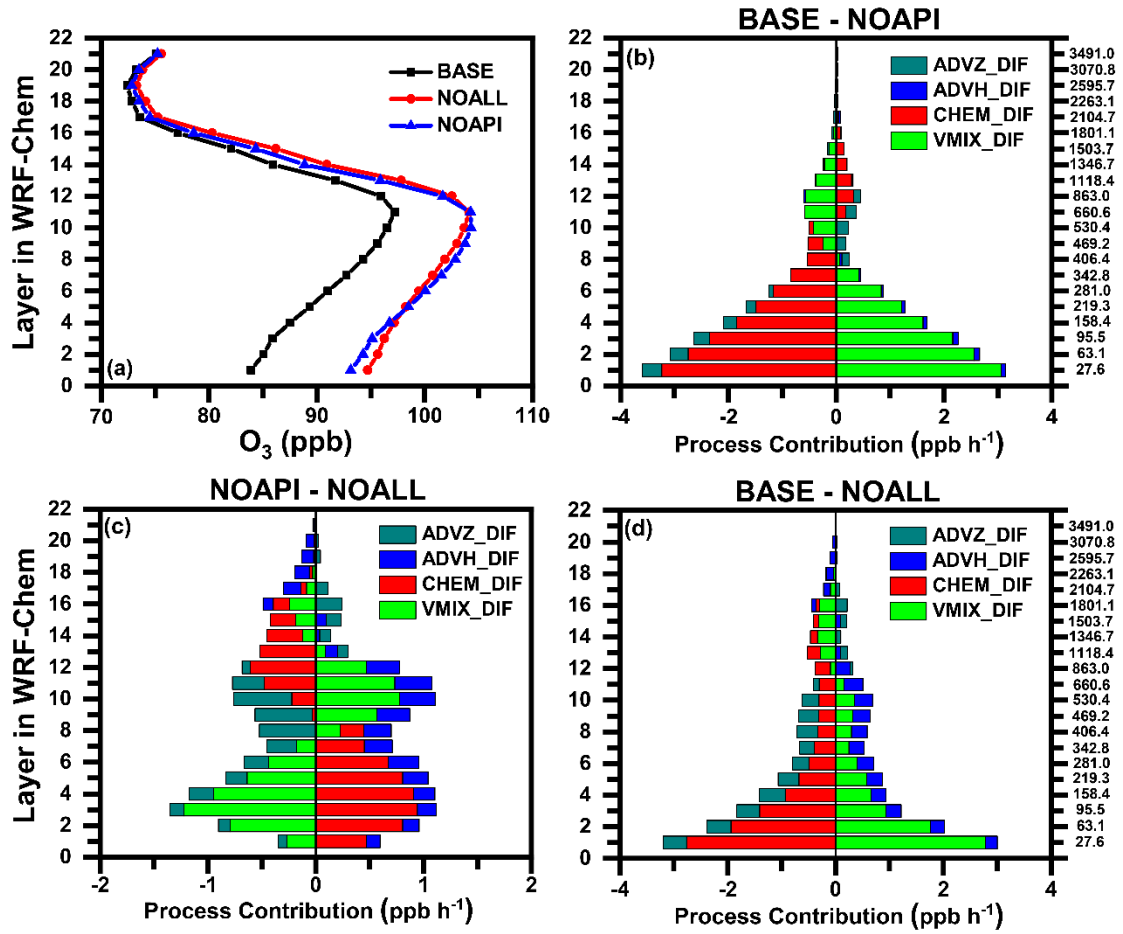


Figure 8. The impacts of aerosol-radiation interactions on vertical O₃ averaged over the three episodes. (a) Vertical profiles of simulated O₃ concentrations in BASE (black dotted line), NOAPI (blue dotted line), and NOALL (red dotted line) cases over CAPAs. (b-d) Changes in O₃ budget due to API, ARF, and ALL over CAPAs during the daytime (08:00-17:00 LST). Differences of each process contribution are denoted by ADVZ_DIF, ADVH_DIF, CHEM_DIF, and VMIX_DIF.